HHS Public Access

Author manuscript

*Science*. Author manuscript; available in PMC 2021 May 13.

Published in final edited form as:

*Science*. 2020 January 17; 367(6475): 301–305. doi:10.1126/science.aaw9544.

# Lipid-gated monovalent ion fluxes regulate endocytic traffic and support immune surveillance

**Spencer A. Freeman**[#1,*], **Stefan Uderhardt**[#2], **Amra Saric**[#3], **Richard F. Collins**[1], **Catherine M. Buckley**[1,4], **Sivakami Mylvaganam**[1], **Parastoo Boroumand**[1], **Jonathan Plumb**[1], **Ronald N. Germain**[2], **Dejian Ren**[5], **Sergio Grinstein**[1,6,*]

[1]Program in Cell Biology, Peter Gilgan Centre for Research and Learning, Hospital for Sick Children, 686 Bay Street, 19-9800, Toronto, ON, M5G 0A4, Canada.

[2]Lymphocyte Biology Section, Laboratory of Immune System Biology, National Institute of Allergy and Infectious Diseases, National Institutes of Health, Bethesda, Maryland, USA.

[3]Neurosciences and Cellular and Structural Biology Division, Eunice Kennedy Shriver National Institute of Child Health and Human Development, National Institutes of Health, Bethesda, Maryland, USA.

[4]Institute of Microbiology and Infection and School of Biosciences, University of Birmingham, Edgbaston, Birmingham, UK.

[5]Department of Biology, University of Pennsylvania, 415 South University Avenue, Philadelphia, Pennsylvania, USA.

[6]Keenan Research Centre of the Li Ka Shing Knowledge Institute, St. Michael's Hospital, 290 Victoria Street, Toronto, ON, Canada, M5C 1N8.

[#] These authors contributed equally to this work.

## Abstract

Despite ongoing (macro)pinocytosis of extracellular fluid, the volume of the endocytic pathway remains unchanged. To investigate the underlying mechanism, we used high-resolution video imaging to analyze the fate of macropinosomes formed by macrophages in vitro and in situ. $Na^+$, the primary cationic osmolyte internalized, exited endocytic vacuoles via two pore channels (TPC), accompanied by parallel efflux of $Cl^-$ and osmotically-coupled water. The resulting shrinkage caused crenation of the membrane which fostered recruitment of curvature-sensing proteins. These proteins stabilized tubules and promoted their elongation, driving vacuolar remodeling, receptor recycling, and resolution of the organelles. Failure to resolve internalized fluid impairs the tissue surveillance activity of resident macrophages. Thus, osmotically-driven increases in the surface-to-volume ratio of endomembranes promote traffic between compartments and help to ensure tissue homeostasis.

---

During endocytosis, cells internalize membrane along with extracellular fluid (pinocytosis). The amount of fluid ingested can be substantial: dendritic cells and macrophages take up the

[*]Correspondence to: Spencer Freeman (spencer.freeman@sickkids.ca) or Sergio Grinstein (sergio.grinstein@sickkids.ca).

equivalent of their entire cellular volume every 4 hours (1). Despite continuous uptake of large amounts of water and osmolytes, the endocytic pathway and the cells as a whole retain their volume and ionic composition over extended periods (1). To investigate endomembrane volume and ionic regulation, we chose macropinosomes, large (up to 5 μm) vacuoles formed by specialized cell types (2, 3) (Figs. 1, S1A-B). Unlike smaller endocytic vesicles, macropinosomes can be resolved by diffraction-limited microscopy (4), enabling detailed assessment of their volume as they mature. Moreover, the volume of medium entrapped by macropinosomes is sufficiently large to alter the overall ionic composition of the cells (Fig. S1C-D). When stimulated by macrophage colony stimulating factor (M-CSF), bone marrow-derived macrophages (BMDM) underwent a large burst of macropinocytosis. Multiple (10-15/cell), large vacuoles (mean volume 7 $\mu m^3$) form within 5 min (Figs. 1A, S1A-B). The volume of fluid internalized was equivalent to ≈25% of the cell volume, an increase detectable by electronic cell sizing (Fig. 1B). When visualized using rhodamine-dextran (70 kDa), the macropinosomes of BMDM (Fig. 1A), as well as those formed by peritoneal macrophages and human monocyte-derived macrophages (Fig. S1E), resorbed within 30 min and cell volume returned to basal levels (Fig. 1B). Shrinkage of macropinocytic vacuoles was also observed in vivo. Two-photon imaging of live mice revealed that resident tissue macrophages (RTM) of the peritoneal serosa –interstitial, non-migratory cells that constitutively sample the surrounding milieu ((5), Video S1)– formed large macropinosomes that subsequently contracted (Fig. 1C-D and Video S2).

Macropinosome shrinkage was accompanied by an increase in the intensity of the luminal dextran fluorescence (Fig. 1A), implying that fluid was extracted from the vacuoles. This suggested that the volume loss of the vacuoles is caused by osmotically-driven solvent loss. $Na^+$ and $Cl^-$ constitute the majority of the osmolytes in the fluid engulfed during macropinocytosis. Accordingly, inducing macropinocytosis with M-CSF resulted in a 4-fold increase in the total cellular $Na^+$ content (Fig. S1D). Thus, loss of $Na^+$ and $Cl^-$, along with osmotically-coupled water may underlie the rapid shrinkage of macropinosomes. This was validated by ion substitution experiments: replacing $Na^+$ for the impermeant cation, N-methyl-D-glucamine$^+$ ($NMG^+$), virtually eliminated macropinosome resolution (Figs. 1E, S1E-F, and Video S3). Similarly, shrinkage was precluded when substituting the impermeant anion gluconate$^-$ for $Cl^-$, implying that electroneutrality needs to be maintained during solute export (Figs. 1E, S1E-F). Preventing monovalent ion efflux from macropinosomes also prevented restoration of the cell volume (Fig. S1G). The absence of luminal $Ca^{2+}$ did not prevent macropinosome resolution (Fig. 1E).

We tested a series of ion transport inhibitors to gain insight into the pathways involved in macropinosome shrinkage. Tetrandrine, a potent inhibitor of two-pore channels (TPC) (6), impaired the volume loss (Figs. 2A, S2A-B; Video S4). Interestingly, the endomembrane isoforms TPC1 and TPC2 are expressed at particularly high levels in myeloid cells, including BMDM (Fig. S6I and (7)). Moreover, TPC1 is highly expressed in the macropinocytic interstitial (Ccr2-negative, CD169-positive) RTM, compared to neighboring stromal or migratory (Ccr2-positive, CD169-negative) myeloid cells that are non-macropinocytic (Fig. 2D-E) (5). While undetectable at the plasma membrane, TPC1 was rapidly (≤1 min) acquired by nascent macropinosomes (Fig. 2F), while TPC2 was recruited later (Fig. S3D). BMDM from *Tpc1;Tpc2* double-knockout mice formed large

macropinosomes when stimulated by M-CSF, but these did not shrink and resolve during the course of our analyses (Fig. 2B-C). Using single knock-out mice and RNA interference, we discerned this effect to be attributable primarily to TPC1 (Figs. 2C, S3F-G).

Certain ion channels, including TPCs and TRPMLs, require PtdIns(3,5)$P_2$ for activation (8, 9); this phosphoinositide is generated by phosphorylation of PtdIns[3]P by PIKfyve (10). Consistent with this sequence, PtdIns(3)P and PIKfyve itself were readily detectable on the cytosolic leaflet of nascent macropinosomes (Fig. 2F, S3E). 2xMLN-GFP, a putative probe for PtdIns(3,5)$P_2$ (11) was also found in macropinosomes (Fig. S3E). Macropinosome shrinkage –whether measured directly or assessed indirectly from the overall cell volume gain– was blocked by PIKfyve antagonists (Figs. 2G-I, S1L-N). Inhibiting PIKfyve did not alter the water permeability or pliability of the membrane as indicated by the acute volume loss induced by water abstraction caused by hypertonic medium (Fig. S1K-L). A similar response to hypertonicity was observed in macropinosomes formed in $Na^+$-free solution (Fig. S1J). Despite the fact that TRPML1 channels are recruited to maturing macropinosomes, deletion of the *Trpml1* gene was without effect on macropinosome resorption (Figs. 2C, S3D).

The area of the vacuolar membrane was reduced during shrinkage by emission and severing of tubules and vesicles, which were visualized using FM1-43 (Fig. 3A) or sulforhodamine B (Fig. 3D). Tubule extension accompanies and requires the volume loss that is driven by the export of ions and osmotically-coupled water. Accordingly, substitution of $Na^+$ with $NMG^+$, or blockade of TPC channels by tetrandrine or their inactivation by depleting PtdIns(3,5)$P_2$ impaired tubulation and vesiculation (Fig. 3A-B). Genetic deletion of TPC channels also precluded tubulation (Fig. 3C). Applying a hypertonic solution to macropinosomes that initially failed to shrink because they were loaded with $NMG^+$ or formed in cells treated with a PIKfyve inhibitor revealed that tubulation is a consequence not a cause of volume loss (Figs. 3D-E and Video S5). The tubules emanating from early macropinosomes are remarkably thin, with a modal diameter of ≈30 nm (Fig. 3F, S4C), which likely explains the preferential retention and progressive concentration of large (70 kDa) dextran in the vacuolar lumen. The diameter of the tubules generated during macropinosome resorption is well suited for them to associate with proteins containing BAR domains, concave structures that preferentially bind and stabilize curved membranes of ≈22 nm diameter (12). Indeed, the BAR domain-containing proteins SNX1, SNX2, and SNX5 decorated the tubules emanating from resorbing macropinosomes (Fig. S4A, (13)). Thus, membrane crenation caused by the volume loss potentially generated the necessary curvature to stabilize BAR domains on the membrane and thereby fostered tubulation (Fig. 3I). This notion was tested by generating liposomes and monitoring the effects of hydrostatic tension on the ability of a recombinant BAR-domain protein, BIN1, to induce tubulation. These experiments revealed an exquisite relationship between volume loss and BAR-mediated tubulation: the relief of hydrostatic tension greatly amplified tubulation by BIN1, while swelling the liposomes counteracted it (Figs. 3G, S4D). Given their functional redundancy and ability to form interchangeable heterodimeric complexes, the loss of any one BAR protein is unlikely to prevent tubulation. Because many BAR-domain proteins (including various SNX isoforms) require PtdIns(3)P for optimal binding, we interfered with their association by scavenging the available head-groups of the phosphoinositide by expressing tandem FYVE domains. Indeed, high affinity

(multi-copy) FYVE-domain tandems prevented SNX recruitment and precluded tubulation/resolution of the macropinosomes (Figs. 3H, S4B).

The significance of endomembrane shrinkage driven by efflux of monovalent ions is far-reaching. The resulting tubulation mediates the recycling of plasmalemmal components that are internalized in the course of macropinocytosis and endocytosis. One such example is Mac-1 (αMβ2), an integrin that is key to macrophage adherence, migration and phagocytosis (14). Blocking TPC channels by inhibiting PtdIns(3,5)$P_2$ formation led to a pronounced depletion of plasmalemmal Mac-1, which was instead trapped in endomembrane vacuoles (Fig. 4A, S5C). The effect was phenocopied by simply substituting extracellular $Na^+$ by $K^+$, demonstrating that a $Na^+$ gradient is exploited by the endocytic pathway to direct membrane traffic (Fig. S5A-C). Moreover, non-macropinocytic cells (e.g. fibroblasts) also required $Na^+$ efflux to execute canonical receptor recycling (Fig. S6A-D, G-H) (15, 16). Defective plasmalemmal protein recycling caused by ion substitution had acute functional consequences: the ability of BMDM to bind and ingest complement-coated targets and of fibroblasts to form focal adhesions –processes mediated by integrins– were severely depressed (Figs. S5D-E, S6E-F).

The need for ion efflux from endocytic compartments for normal cell function was also documented in situ. When $Na^+$ efflux from the endocytic pathway was prevented in vivo, the ability of interstitial RTM to survey their environment was impaired (Fig. 4B-E, Video S6). Blocking β1 and β2 integrins similarly inhibited surveillance (Fig. S7A-C). When microlesions are made by targeted laser ablation to adjacent fibroblasts, RTM normally emit processes to contain the damage (5), preventing the recruitment and activation of neutrophils. When PIKfyve or TPCs were inhibited, the cells failed to resorb vacuoles and were unable to respond to the damage (Fig. 4D-E). As a result, neutrophil swarming ensued (Fig. 4F-G). Thus, vacuole resolution, mediated by lipid-gated $Na^+$ efflux, underpins membrane traffic necessary to maintain cellular responsiveness.

Because macropinocytosis is not restricted to phagocytes, inhibition of vacuolar shrinkage affects also other cell types (17). HT1080 fibrosarcoma cells display vigorous constitutive macropinocytosis (Fig. 4H), express TPC1 at comparatively high levels (Fig. S8A) and localize the channel to macropinosomes (Fig. 4H). HT1080 cells require growth factors for survival and are highly responsive to EGF. Because the EGF receptor is internalized along with the macropinosomal membrane, effective recycling to the cell surface is key. Preventing vacuole shrinkage resulted in the depletion of EGF receptors from the plasmalemma (Fig. S8B) and this was associated with reduced responsiveness to EGF and delayed growth (Fig. 4I-J, S8C).

Solute transport may be involved in the shrinkage and tubulation of other organelles. In this regard, lysosomes are known to undergo swelling in cells treated with PIKfyve antagonists (18). Impaired solute extrusion could account for the volume gain, which is compounded by ongoing membrane fusion that is uncompensated by shrinkage-dependent tubulation and/or vesiculation and scission. Indeed, lysosomes swollen by inhibition of PIKfyve recovered their ability to tubulate when exposed to hypertonic solution (Video S7), and also upon removal of the PIKfyve inhibitor, but failed to do so when tetrandrine was present (Fig.

S9A-E). Overexpression of TPC2 alone caused lysosomes to become more tubular, suggesting the channel may be involved in these processes (Fig. S10A-C, Video S8).

In summary, we propose a role for ion fluxes in the endocytic pathway: extrusion of osmotically abundant ions/solutes, accompanied by water, cause vacuolar/vesicular shrinkage leading to crenation of the membrane, forming convex protrusions that stabilize proteins with BAR or similar curvature-sensing domains. These, in turn, foster tubulation and eventual scission that is critical for inter-organellar traffic. In macrophages that continuously survey the extracellular space, an ongoing ion efflux from the endocytic pathway drives the resolution of fluid that is taken up during this process, supporting recycling of receptors to maintain their function. Thus, the resolution of organelles formed during surveillance is necessary to preserve tissue integrity.

## Materials and Methods

### Cell isolation, culture, and transfection

Murine macrophages were harvested from the marrow of long bones from 6- to 10-week old C57Bl/6 wild-type mice. Cells were washed in PBS before culturing in DMEM containing L-glutamine, 10% heat-inactivated serum, and 10% L929 fibroblast-conditioned medium as a source of macrophage colony-stimulating factor (M-CSF). For primary macrophage transfections, after 5-6 days of culture, cells were lifted with 5 mM EDTA in PBS, centrifuged, and resuspended in T buffer from the Neon™ transfection system (ThermoFisher). 1-5 μg of plasmid DNA or 100 pM siRNA was added to $2x10^6$ cells in 120 μL of T buffer before a single 1500 V, 30 ms pulse was applied through the suspension. For fluorescence microscopy, cells were imaged 4-8 h after transfection. For knockdown experiments, cells were lifted and transfected a second time after 24 h, and then used after 48 h. These approaches routinely resulted in 10-25% transfection efficiency of plasmid DNA as determined by fluorescence microscopy and a 60-90% reduction in mRNA caused by siRNA, as determined by qPCR, respectively.

HT1080 cells from ATCC (CCL-121) were cultured in DMEM containing L-glutamine and 10% heat-inactivated serum. Growth assays were done in medium with low L-glutamine (0.2 mM), 5% FBS, and 2% albumin. Mouse embryonic fibroblasts were from ATCC (SCRC-1008) and cultured in DMEM containing L-glutamine and 5% heat-inactivated serum.

### Animal Studies

The following mouse strains were used in this study:

- $Lyz2^{Cre/Cre}$ (B6.Cg-Gt(ROSA)26Sortm14(CAG-tdTomato)Hze/J; The Jackson Laboratories; 007914).
- $tdTom^{fl/fl}$ (B6N.129P2(B6)-Lyz2tm1(cre)Ifo/J; The Jackson Laboratories; 018956).
- F1 crossbreed of the above was used for experiments designated “LysM-tomato”.

- *Tpc1*$^{-/-}$: The *Tpc1* knockout was generated from an ES cell line developed by Velocigene (clone # 13234, purchased from KOMP) to delete the open reading frame. Mice were backcrossed to C57BL/6 (Jax) for more than 10 generations. Genotyping was done using a mixture of three primers with sequences of AGAACACGTTCATCAGTAACGATTATG (forward), AAAGCTGTGTCAGAAGTGAGGGACC (reverse 1) and TCTGTCTGTCCTAGCTTCCTCACTG (reverse 2). The PCR condition was 94°C 2'; (94°C 30"; 55°C 30"; 72 °C 30") x35; 72°C 5'. Primers amplify the wild-type as 595 bp and the knockout as 381 bp.
- *Tpc2*$^{-/-}$: The generation of *Tpc2* knockout was previously described (1).
- *Tpc1*$^{-/-}$;*Tpc2*$^{-/-}$: The double knockout was generated by crossing the individual knockouts.
- *Trpml1*$^{-/-}$: The generation of *Trpml1* knockout was previously described (2) using crosses of heterozygous mice from S. Slaughenhaupt (Center for Human Genetic Research, Massachusetts General Hospital at Harvard Medical School) and provided by Dr. N. Jones (The Hospital for Sick Children).
- C57BL/6J (The Jackson Laboratories; 000664).

Mice used for cell isolation experiments were maintained under a 12:12-h light:dark cycle, and were provided with food and water *ad libitum*. All animal study protocols were approved by the animal care committee of The Hospital for Sick Children.

Reporter mice for intravital imaging were maintained in specific pathogen-free conditions at an American Association for Laboratory Animal Care–accredited animal facility at the NIAID (National Institute of Allergy and Infectious Diseases, NIH) and were used under a study protocol approved by the NIAID Animal Care and Use Committee (National Institutes of Health, NIH). All imaging experiments were performed with 8-12-week old mice, and both males and females were used at equal ratios for the studies as they displayed similar immune cell dynamics *in vivo*.

### Intravital imaging of the peritoneal serosa

Intravital microscopy was performed as previously described (3). In brief, a midline incision of the abdominal wall of anesthetized mice (Isoflurane; Baxter; FORANE; Cat#1001936040) was performed and the parietal peritoneal serosa was exposed. 10 μL of buffer (pre-warmed HBSS containing 2 mM $CaCl_2$ and 1 mM $MgCl_2$; pH 7.4; 34°C) with inhibitors/vehicle or antibodies was applied topically, before installing a sterilized cover glass (Fisher Scientific; Cat# 12-545-80) and transferring the animal to a heated (36°C) imaging chamber.

To assess endosome resolution in RTM in vivo, YM-201636 (CAS 371942-69-7; Cayman Chemical; dissolved in DMSO; final stock concentration 10 mM), tetrandrine (CAS 518-34-3; Abcam; dissolved in DMSO: final stock concentration 5 mM) or vehicle alone (DMSO) were applied topically and incubated for 30 min. Then, mM-CSF (PeproTech; dissolved in $H_20$; final concentration 100 ng/mL) was added and incubated for another 10

min. To remove M-CSF, the tissue was then carefully washed three times with 1 mL pre-warmed buffer before installing a fresh cover glass with 10 μL buffer. Imaging was started after an additional 30 min incubation time to allow for endosome resolution. The emission of second-harmonic light from non-centrosymmetric structures (matrix, e.g. collagen) was also collected.

To assess integrin function, 1 μg of each anti-CD29 (HMβ1-1; BioLegend; #102235) plus anti-CD11b/β2 integrin (M1/70; BioLegend; #101213) or isotype controls (Armenian hamster IgG plus rat IgG2b) were applied topically, and imaging was started after 30 min incubation time. Tissue staining was done with anti-CD11b and anti-CD169/Siglec-1 (3D6.112; BioLegend; #142407). Imaging was performed on a Zeiss 710 microscope equipped with a Chameleon femtosecond-pulsed laser (Coherent; 930 nm wavelength) and a 20x water immersion objective (NA 1.0; Zeiss). Raw imaging data were processed and analyzed with Imaris 9.2.1 (Bitplane). Macrophage probing dynamics were recorded over 30 min (resolution 512x512; 16 bit; Z- stacks of 12 focal planes each 3 μm apart; frame rate 968 ms; 128 imaging frames in total) and fluorescent intensities from all frames were binarized and summed to visualize and calculate overall tissue surveillance over time using Adobe Photoshop (CC 2019).

To measure individual endosome volumes, still images of macrophages were recorded at indicated time points at higher magnification (4-5x zoom) and resolution (resolution 1024x1024; 16 bit; Z-stacks with 0.5 μm step size). Diameter measurements were performed after deconvolution (Huygens Professional, version 18.04) using the Imaris slice-viewer mode.

## Sterile laser damage

Sterile laser damage was performed as previously described (3). In brief, after treating the tissue with inhibitors/vehicle as described above, stromal microlesions (partial-to-unicellular damages) were induced with a brief (< 1 s) two-photon laser pulse using a 20x objective at a 35x zoom.

Macrophage dynamics were recorded immediately after damage induction for 30 min (to assess damage response; “cloaking”) or up to 3 h (to assess endogenous neutrophil response; “swarming”). Spatiotemporal coordinates of individual macrophage pseudopods were used to calculate track displacements in Imaris.

To assess neutrophil damage responses (swarming vs. no swarming), 6 individual microlesions were induced each 1000 μm apart, and static images were recorded every 20 min over 3 h. Neutrophils were identified in $LysM^{gfp/gfp}$ mice by morphology and GFP intensity. Formation of neutrophil clusters at the site of the microlesion was assessed as neutrophil swarming activity.

Intravital imaging experiments were performed using $LysM^{gfp/gfp}$ (NIAID repository, Taconic Farms, Cat#000342) or $LysM^{Cre/+}$ $tdTomato^{fl/+}$ mice (The Jackson Laboratories; Cat#007914 crossed with Cat#018956) at ages 8-10 weeks, with similar results in males and females.

### Generation of TPC1 KO HT1080 by CRISPR/Cas9

A CRISPR/Cas9 and a dual-sgRNA strategy was implemented to inactivate the *Tpc1* gene. Two sgRNA sequences (CTAGAAGATGCCTCTAATGG and ATCCTGACCTTGGATGAGGG) flanking the start site of TPC1 within exon 3 were chosen (using the online tool https://benchling.com) and synthesized (Eurofins Genomics). The 2 guides were individually cloned into pX458 vector (Addgene #48538) as described (4) and verified by Sanger sequencing (Eurofins Genomics). The vectors were co-transfected into HT1080 cells and 24 h later the cells were bulk-sorted by FACS based on $GFP^+$ signal. The sorted cells were allowed to recover and grow for 3 days, then diluted and re-plated to achieve well-separated single cells. After 2 weeks in culture, individual colonies were picked by pipette and expanded for ≈1 week in larger wells. Cells were screened by extracting genomic DNA with KAPA Express Extract (KAPA Biosystems, Cat# KK7103) and carrying out PCR with the forward primer 5'AGTATTTGTTCTTGCAGGGTTCC and reverse primer 5'AGGGAAGGCAGCCAAAGTAG to yield a product of approximately 1800 bp in WT cells and 1660 bp in CRISPR-edited cells.

### Cell sorting and RNA sequencing

RNA sequencing protocol has been published previously (3) and the RNAseq data pooled from three independent biological replicates have been deposited online (NCBI GEO: CGSE119870). In brief, Cx3cr1 GFP/+ Ccr2 RFP/+ mice received an i.v. injection of Dextran-Cascade Blue (Invitrogen; #D1976) to label pinocytosing cells in the interstitium of the peritoneal serosa. Intravascular leukocytes were labeled by i.v. injection of anti-CD45 (BioLegend; clone 30-F11) 3 min prior to euthanasia. The peritoneal serosa was harvested and digested for 20 min at 37°C in RPMI (GIBCO; Cat#11875093) with 1% FBS (Gemini; Lot#A20G001; Cat#100-106), 250 μg/ml Liberase TL (Sigma-Aldrich; Cat#5401020001), 100 μg/mL DNase II (Sigma-Aldrich; Cat# D8764), 25 μM Z-VAD-FMK (Tocris; Cat#2163) and 10 mM HEPES (GIBCO; Cat#15630080). Cells were resuspended in PBS (GIBCO; Cat#10010-23; Lot#1943335) with 2% FBS, 2 mM EDTA (Quality Biological; Cat#51-027-101) and 25 μM Z-VAD-FMK and stained for CD11b (BioLegend; clone M1/70), I-A/I-E (BioLegend; clone M5/114.15.2) and Ly6G (BioLegend; clone 1A8). $CD45^-$ $CD11b^+$ $Ly6G^-$ cells were sorted into $Dextran^+$ $MHCII^{+/-}$ $CCR2^-$ $CX3CR1^{+/-}$ (sessile RTM) and $Dextran^-$ $MHCII^+$ $CCR2^+$ $CX3CR1^-$ (migratory monocytes), directly into 0.5 mL TRIZOL (Invitrogen; Cat#15596026) using a FACS-Aria cell sorter (BD Bioscience).

A Nugen Ovation SoLo kit (NuGEN; Cat#0501-32) was used to generate RNAseq libraries with an input of ≈1 ng total RNA. Sequencing was performed using Illumina NextSeq V2 reagents (Illumina; Cat#FC-404-2005) with pair end 75 pair reads at a sequencing depth of ~ 20 million reads. Reads were mapped to Mus musculus mm10 genome build (UCSC annotation) and Salmon-estimated transcript-per-million values were summarized at the gene level using tximport (v 1.4.0) and the org.Mm.eg.db database.

### Additional reagents and plasmids

YM201636 (Cayman Chemical, 371942-69-7) was used at 500 nM. Apilimod (Santa Cruz, sc-40051) was used at 500 nM. WX8 (a generous gift from Dr. M. DePamphilis, NIH) was

used at 500 nM (5). Ouabain octahydrate (Sigma Aldrich, O3125) was used at 5 mM. Furosemide (Tocris, 3109) was used at 5 μM. Bumetanide (Tocris, 3108) was used at 5 μM. 4,4'-diisothiocyanatostilbene-2-2'-disulfonic acid disodium salt (DIDS, Sigma Aldrich, D3514) was used at 10 μM. CFTRinh-172 (Tocris, 3420) was used at 1 μM. NPPB (Tocris, 0593) was used at 10 μM. Tetrandrine (Abcam, ab142464) was used at the indicated concentrations. Nocodazole (Sigma, 487928) was used at 5 μM.

mTPCN1 stealth siRNA (cat #MSS217431), murine and human TPCN1/TPCN2/ABT1 TaqMan® probes (Mm00455326_m1, Hs01552053_g1, Hs00330542_m1, Mm00803824_m1, Hs00706003_s1), TaqMan® RT-PCR master mix (4444557) were from ThermoFisher. The generation of plasmids used for the expression of LAMP-1-RFP and tubulin-GFP (6), SNX2-GFP (7), and PX-GFP (8) is described in the references provided. hTPC1wt-tomato was a generous gift from Dr. N. Klugbauer (9). EGFR-GFP was from Dr. A. Sorkin (Addgene plasmid #32751). pEGFP-N3-hTPC2wt was from Dr. S. Di Pietro (Addgene plasmid #80153). PIKfyve-GFP was from Dr. G. van den Bogaart (Addgene plasmid #121148). TRPML1-YFP was from Dr. C. Montell (Addgene plasmid #18826). 2xfyve-GFP, 2xfyve-mCherry, and 5xfyve-GFP were from Dr. L. Cantley (Beth Israel Deaconess Medical Center, Boston, Mass.). Mutagenic primers for TPCN2.K321A were: fw 5'-cggggctacctgatgGCGtctctccagacctcg-3', rv 5'-cgaggtctggagagaCGCcatcaggtagccccg-3'. Sequencing confirmed with the primer 5'-tctggtggactggaccgt-3'. SNX1-GFP was generated by PCR amplification of human SNX1 cDNA using the primers 5' GATCTCGAGCTCAAGCTTCGATGGCGTCGGGTGGTGGTG and 5' GTACCGTCGACTGCAGAATTGGGGAGATGGCCTTTGCC and performing Gibson assembly (New England Biolabs, Cat# E2611) with an EcoRI-digested pEGFP-N1 vector.

Anti-Mac-1 antibody was from BD Bioscience (550282). Anti-β-tubulin was from Sigma (T6199). Anti-EEA1 antibody was from Santa Cruz (sc-6415). Anti-paxillin was from BD Bioscience (610051). Anti-β1-integrin (TS2/16) (303002), anti-CD11b (M1/70) (101201), and CD29 (HMβ1) (102201) were from BioLegend.

All lipids were from Avanti Polar Lipids Inc.: total porcine brain extract (13110P), PE-rhodamine (810150P), PtdIns(4,5)$P_2$ (850185). Alexa568-Tfn was from ThermoFisher (T23365).

## Macropinocytosis

Macrophages were seeded onto glass coverslips for 24-48 h at high confluency. The medium was then removed and replaced with solutions warmed to 37°C of either PBS with $Ca^{2+}$ and $Mg^{2+}$, or buffers containing 150 mM of either NaCl, N-methylglucamine-chloride, or Na-gluconate, plus 1 mM $MgCl_2$, 1 mM $CaCl_2$, 5 mM KCl, 20 mM HEPES, pH 7.2. The osmolarity of the solutions was equivalent (≈300 mOsm) as measured using a model 5004 automatic osmometer (Precision Systems; 2094). Each solution also contained 70,000 MW tetramethylrhodamine- or Oregon Green-dextran (ThermoFisher, D1818 or D7173) to identify the newly formed vacuoles, and 100 ng/mL recombinant murine M-CSF (Peprotech, cat. # 315-02) to stimulate macropinocytosis.

In some cases, FM1-43 dye (ThermoFisher, T35356) was added to label the membrane, or high molecular weight dextran was substituted with sulforhodamine B (Sigma-Aldrich, 230162). Where specified, inhibitors were added to the macrophages at the indicated concentrations 5 min before the addition of M-CSF. After 5 min of M-CSF stimulation, cells were washed and vacuole resolution was monitored by spinning-disc microscopy as described previously (10) in PBS with or without inhibitors. The mean macropinosomal volume and dextran intensity were determined using Volocity software (PerkinElmer), excluding objects below 0.5 $\mu m^3$.

In experiments where macropinosomes were treated with PIKfyve inhibitors or loaded with $NMG^+$ and sulforhodamine B, then induced to tubulate by elevating the tonicity of the media, the sulforhodamine B was loaded at 1 μg/mL. After 10 min post-macropinosome sealing, an 800 mOsm, pH 7.2 solution of NaCl was used at 1:1 to adjust the tonicity to 500 mOsm overall. In experiments where hypotonic solutions were used, the medium was adjusted using 4:1 solution 100 mOsm NaCl, pH 7.2.

## Cell volume measurements

Macrophages seeded on non-treated Petri dishes were lifted mechanically. The median cell diameter for >5000 cells was determined using the Z2 Coulter particle count and size analyzer (Beckman Coulter) and converted to volume by assuming that the suspended cells were spherical.

## Atomic absorption spectrometry

Differentiated BMDM were seeded onto 6-well plastic TC dishes and cultured for an additional 24 h. Cells were counted by imaging 3 fields by phase microscopy. After stimulation, dishes were washed x3 by gentle, brief submersion of the dishes in $Na^+$-free solutions to remove contaminating ions. Cells were lysed with 1 mL $H_2O$ containing 1% $HNO_3$ and 0.1% LiCl. Lysis was done by scraping and vigorous pipetting. Samples were analyzed using a PinAAcle 900T Atomic Absorption Spectrometer (PerkinElmer).

## STED microscopy

STED microscopy was performed as previously described (11). Briefly, using a Leica TCS SP8 STED 3X microscope, images were acquired using HyD detectors and a 90X/1.4 glycerol objective. Samples were labeled with Cy3-conjugated secondary antibodies and excited at 554 nm using a white-light laser. Emissions were time-gated 0.5-6 ns. A 1.5 W depletion laser at 660 nm was used for the red channel, at 45% of maximal power. Images were acquired using Leica LAS X software with a xy pixel size of 31 nm and z step of 200 nm and then deconvolved with Leica Lightning software (Scientific Volume Imaging, The Netherlands).

## Liposome generation and tubulation

Liposomes were made as previously described (12). Briefly, whole brain lipid (porcine) at 94% of the total lipid concentration, PtdIns(4,5)$P_2$ at 5% and PE-rhodamine at 1% were mixed in chloroform and the solvent was removed under a stream of nitrogen. Liposomes were generated by vortexing into 20 mM Tris-HCl and sonication in an ice-bath, then

incubated with 20 μg/mL recombinant human BIN1 protein (Abcam, 98238) on ice for 30 min. Liposomes were then seeded onto acid-washed glass coverslips coated with a 1:1000 solution of poly-L-lysine in 20 mM Tris-HCl (Sigma, P4707) for 10 min and imaged by spinning-disc microscopy. The osmolarity of the solution was then adjusted with Tris-HCl containing NaCl or water and liposomes were again imaged 30 sec later. Objects were identified and the mean aspect ratio, equal to the major axis/minor axis of each liposome with a fitted ellipse, was determined using ImageJ software.

### Immunoblotting

HT1080 cells were serum-starved for 2 h in DMEM, then given 100 ng/mL human recombinant EGF (Sigma Aldrich, E9644) for the indicated times and lysed in RIPA buffer containing protease and phosphatase inhibitors. Laemmli sample buffer with 2-mercaptoethanol was added to the cell lysates, samples were boiled for 5 min, then run on 10% polyacrylamide gels. Blots were incubated with rabbit p-Ser473-Akt and mouse total-Akt antibodies (Cell Signaling Technology, 736E11 and 40D4) at 1:2000 in TBST overnight. Secondary antibodies conjugated with LI-COR-compatible fluorophores were used for detection on an Odyssey FC imaging system (LI-COR Biosciences).

### Particle Binding

Sheep red blood cells (MP Biomedicals, 55876) were opsonized with rabbit-anti sheep red blood cell IgM, washed, then incubated with C5a-deficient serum (Accurate Chemical & Scientific Corp., AIAM6840). Prior to adding phagocytic targets, the primary murine macrophages were treated with vehicle control, YM201636 at 500 nM, or 10 μM tetrandrine along with M-CSF for 30 min. Binding was determined post-fixation, washing, and permeabilization of the cells by staining the red cells with goat anti-rabbit IgM conjugated with DyLight488 (Abcam, ab96979).

### Transmission electron microscopy

Monolayers of BMDMs grown on glass coverslips were fixed in 2% glutaraldehyde in 0.1 M sodium cacodylate buffer, rinsed in buffer, post-fixed in 1% osmium tetroxide in buffer, dehydrated in a graded ethanol series followed by propylene oxide, and embedded in Quetol-Spurr resin. Sections (90 nm thick) were cut on a Leica Ultracut ultramicrotome, stained with uranyl acetate and lead citrate and viewed in an FEI Tecnai 20 TEM.

### Lysosomal motility

TPC2-GFP-expressing compartments were recorded over 10-30 sec at 10 frames per sec on a Zeiss Axiovert 200M microscope equipped with a 100x, 1.45 N.A. oil objective, a custom 2.4x magnification lens, and a back-thinned EM-CCD camera (Hamamatsu). The motion type for individual lysosomes was determined using an MSS analysis, previously described (13). Directed motion was defined as those lysosomes having linear or super-diffusive trajectories, indicative of motor-based movement of the organelle.

## Supplementary Material

Refer to Web version on PubMed Central for supplementary material.

## Acknowledgements

We thank Kimberley Aranda and Zhengjiang Liu for tissue preparation and genotyping. We are grateful to the Transgenic and Chimeric Mouse Core of the University of Pennsylvania (supported by NIH center grants P30DK050306, P30DK019525, and P30CA016520) for the generation of the TPC1 line. Supported by grant FDN-143202 from CIHR to S.G. This work was also supported in part by the Intramural Research Program of the NIH to R.G. and S.U. and by NIH grants R01 HL147379 and R01 GM133172 to D.R.

## References and Notes

1. Steinman RM, Brodie SE, Cohn ZA, Membrane flow during pinocytosis. A stereologic analysis. J Cell Biol 68, 665–687 (1976). [PubMed: 1030706]
2. Swanson JA, Shaping cups into phagosomes and macropinosomes. Nat Rev Mol Cell Biol 9, 639–649 (2008). [PubMed: 18612320]
3. Swanson JA, Watts C, Macropinocytosis. Trends Cell Biol 5, 424–428 (1995). [PubMed: 14732047]
4. Yoshida S, Hoppe AD, Araki N, Swanson JA, Sequential signaling in plasma-membrane domains during macropinosome formation in macrophages. J Cell Sci 122, 3250–3261 (2009). [PubMed: 19690049]
5. Uderhardt S, Martins AJ, Tsang JS, Lammermann T, Germain RN, Resident Macrophages Cloak Tissue Microlesions to Prevent Neutrophil-Driven Inflammatory Damage. Cell 177, 541–555 e517 (2019). [PubMed: 30955887]
6. Sakurai Y et al., Ebola virus. Two-pore channels control Ebola virus host cell entry and are drug targets for disease treatment. Science 347, 995–998 (2015). [PubMed: 25722412]
7. Lattin JE et al., Expression analysis of G Protein-Coupled Receptors in mouse macrophages. Immunome Res 4, 5 (2008). [PubMed: 18442421]
8. She J et al., Structural insights into the voltage and phospholipid activation of the mammalian TPC1 channel. Nature 556, 130–134 (2018). [PubMed: 29562233]
9. Wang X et al., TPC proteins are phosphoinositide- activated sodium-selective ion channels in endosomes and lysosomes. Cell 151, 372–383 (2012). [PubMed: 23063126]
10. Dove SK et al., Osmotic stress activates phosphatidylinositol-3,5-bisphosphate synthesis. Nature 390, 187–192 (1997). [PubMed: 9367158]
11. Li X et al., Genetically encoded fluorescent probe to visualize intracellular phosphatidylinositol 3,5-bisphosphate localization and dynamics. Proceedings of the National Academy of Sciences of the United States of America 110, 21165–21170 (2013). [PubMed: 24324172]
12. Peter BJ et al., BAR domains as sensors of membrane curvature: the amphiphysin BAR structure. Science 303, 495–499 (2004). [PubMed: 14645856]
13. Kerr MC et al., Visualisation of macropinosome maturation by the recruitment of sorting nexins. J Cell Sci 119, 3967–3980 (2006). [PubMed: 16968745]
14. Dustin ML, Complement Receptors in Myeloid Cell Adhesion and Phagocytosis. Microbiol Spectr 4, (2016).
15. Castonguay J et al., The two-pore channel TPC1 is required for efficient protein processing through early and recycling endosomes. Sci Rep 7, 10038 (2017). [PubMed: 28855648]
16. Grimm C et al., High susceptibility to fatty liver disease in two-pore channel 2-deficient mice. Nature communications 5, 4699 (2014).
17. Commisso C et al., Macropinocytosis of protein is an amino acid supply route in Ras-transformed cells. Nature 497, 633–637 (2013). [PubMed: 23665962]
18. Jefferies HB et al., A selective PIKfyve inhibitor blocks PtdIns(3,5)P(2) production and disrupts endomembrane transport and retroviral budding. EMBO Rep 9, 164–170 (2008). [PubMed: 18188180]
19. Capurro MI et al., VacA generates a protective intracellular reservoir for Helicobacter pylori that is eliminated by activation of the lysosomal calcium channel TRPML1. Nat Microbiol 4, 1411–1423 (2019). [PubMed: 31110360]
20. Ran FA et al., Genome engineering using the CRISPR-Cas9 system. Nat Protoc 8, 2281–2308 (2013). [PubMed: 24157548]

21. Sharma G et al., A family of PIKFYVE inhibitors with therapeutic potential against autophagy-dependent cancer cells disrupt multiple events in lysosome homeostasis. Autophagy 15, 1694–1718 (2019). [PubMed: 30806145]
22. Sherer NM et al., Visualization of retroviral replication in living cells reveals budding into multivesicular bodies. Traffic 4, 785–801 (2003). [PubMed: 14617360]
23. Carlton JG et al., Sorting nexin-2 is associated with tubular elements of the early endosome, but is not essential for retromer-mediated endosome-to-TGN transport. J Cell Sci 118, 4527–4539 (2005). [PubMed: 16179610]
24. Kanai F et al., The PX domains of p47phox and p40phox bind to lipid products of PI(3)K. Nat Cell Biol 3, 675–678 (2001). [PubMed: 11433300]
25. Canton J et al., Calcium-sensing receptors signal constitutive macropinocytosis and facilitate the uptake of NOD2 ligands in macrophages. Nat Commun 7, 11284 (2016). [PubMed: 27050483]
26. Freeman SA et al., Transmembrane Pickets Connect Cyto- and Pericellular Skeletons Forming Barriers to Receptor Engagement. Cell 172, 305–317 e310 (2018). [PubMed: 29328918]
27. Yeung T et al., Membrane phosphatidylserine regulates surface charge and protein localization. Science 319, 210–213 (2008). [PubMed: 18187657]
28. Jaqaman K et al., Robust single-particle tracking in live-cell time-lapse sequences. Nat Methods 5, 695–702 (2008). [PubMed: 18641657]

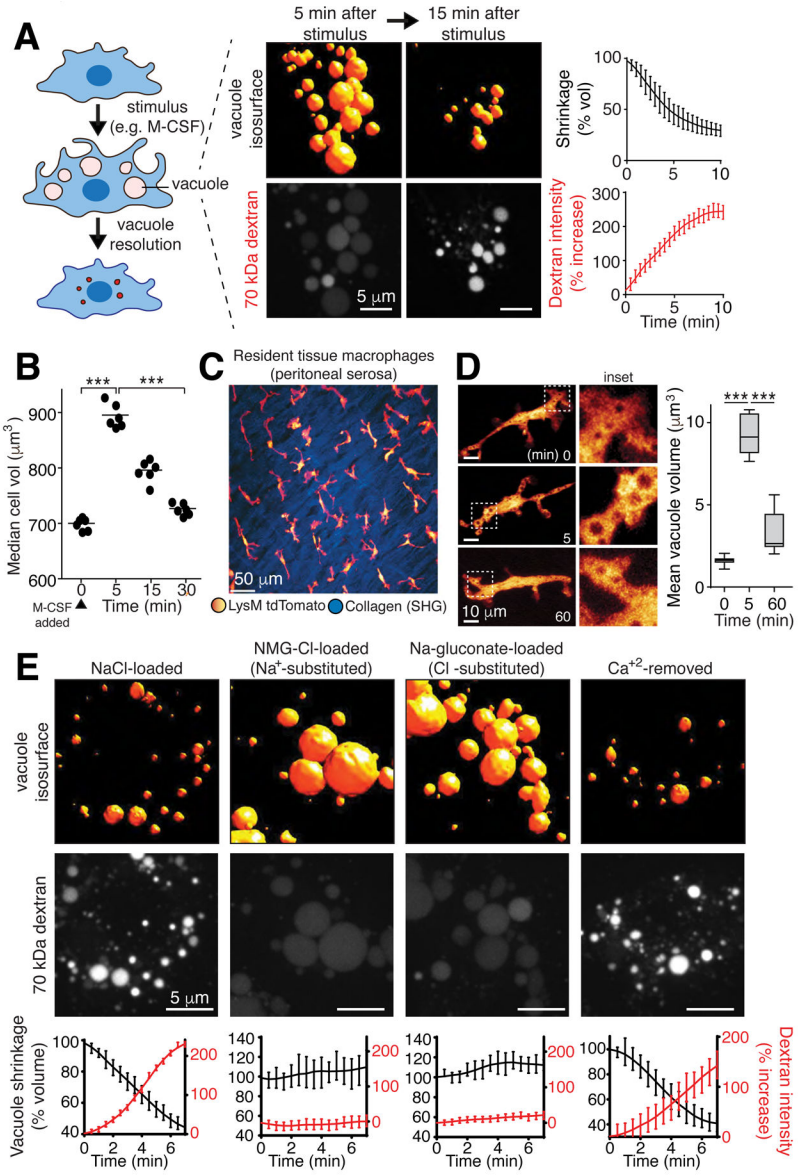


**Figure 1. Vacuolar shrinkage requires monovalent ion efflux.**

**A**, Volume and 70 kDa rhodamine-dextran fluorescence intensity changes of macropinosomes induced in bone marrow derived macrophages (BMDM) by macrophage colony-stimulating factor (M-CSF); data are means ± SEM of >100 vacuoles from 3 independent experiments (i.e. n=3). Measurement of vacuole resolution was initiated after a 5-min stimulation with M-CSF in medium containing dextran, followed by an immediate wash. **B**, Cell (BMDM) volume was measured electronically before and at the indicated times after M-CSF stimulation; $>10^4$ cells per point, n=3. *p* values determined by unpaired, two-sided t-tests. Here and elsewhere *** indicates $p<0.001$, ** is $p<0.01$ and * is $p<0.05$. **C**, Intravital observation of td-Tomato-labeled resident tissue macrophages (RTM; pseudocolored yellow/red) of the peritoneal serosa and second harmonic imaging (SHG) of collagen (blue). See also Videos S1 and S2. **D**, Visualization and volume quantification of M-CSF-induced macropinosomes in RTM in vivo; means, upper and lower quartiles (boxes),

and distribution (whiskers) are graphed. >50 vacuoles, n=3. *p* values determined by Mann-Whitney U test. **E**, Macropinosomes of M-CSF-stimulated BMDM in media containing indicated solutes and dextran. Representative images acquired at 5 min. See also Video S3. Bottom row: mean ± SEM macropinosomal volume and dextran intensity from 3 independent video recordings representing >150 macropinosomes. See also Fig. S1.

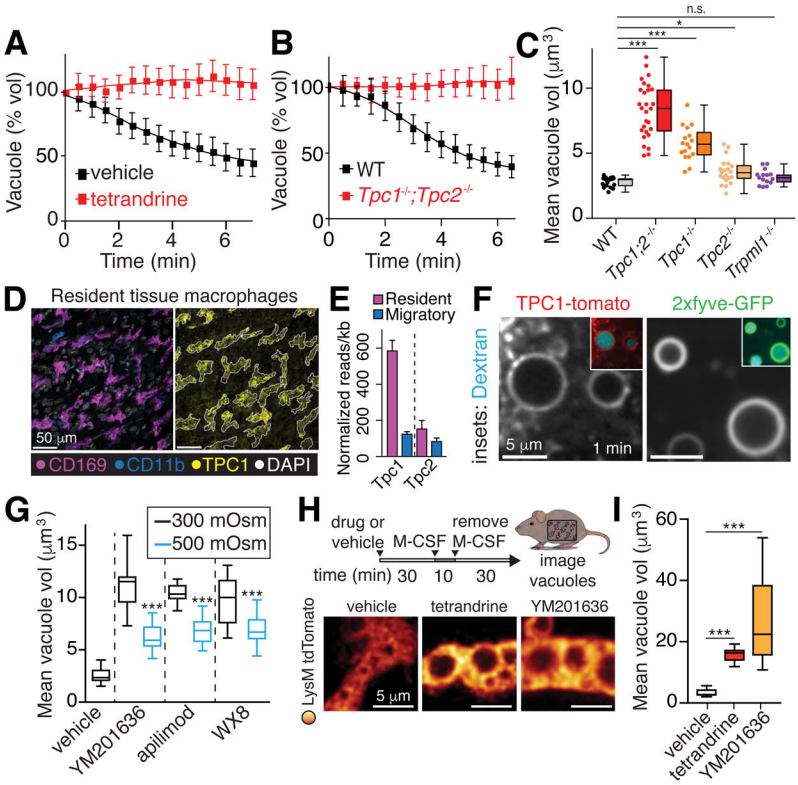


**Figure 2. Monovalent ion efflux mechanisms.**

**A**, Macropinosome volume changes in presence of 5 μM tetrandrine, measured in BMDM. Measurement of vacuole resolution was initiated once cells were washed after a 5-min stimulation with M-CSF in medium containing dextran; tetrandrine or vehicle were present throughout. Means ± SEM, n=3. See also Fig. S2 and Video S4. **B-C**, Macropinosome volume changes following stimulation with M-CSF in *wt, Tpc1/Tpc2* single and double KO, and *Trpml1* KO BMDM. In **C**, means, upper and lower quartiles (boxes), distribution (whiskers), and observations from fields each containing 3-5 cells (dots) measured 10 min after macropinosome formation; n=3. **D**, Staining of the peritoneal serosa. Outline of CD169 signal (left) overlaid on TPC1 signal (right). **E**, RNA-seq. Resident tissue macrophages were $Cx3cr1^{-}/Ccr2^{-}$. Migratory cells were $Cx3cr1^{-}/Ccr2^{+}$. **F**, BMDM expressing TPC1-tomato or 2xfyve-GFP to detect PtdIns(3)P. Dextran shown in cyan. **G**, BMDM stimulated with M-CSF in the presence and 70 kDa rhodamine-dextran and, where indicated, the PIKfyve inhibitors YM201636, apilimod, or WX8 (all used at 500 nM). Resolution was recorded as in **A**. 5 min after iso-osmotic recording, a hyperosmotic solution (final 500 mOsm) was added to verify the osmotic responsiveness of the vacuoles. **H-I**, Visualization and volume quantification of macropinosomes in RTM treated in situ with YM201636 (500 nM) or tetrandrine (5 μM); >15 cells, n=3. All *p* values determined by Mann-Whitney U tests.

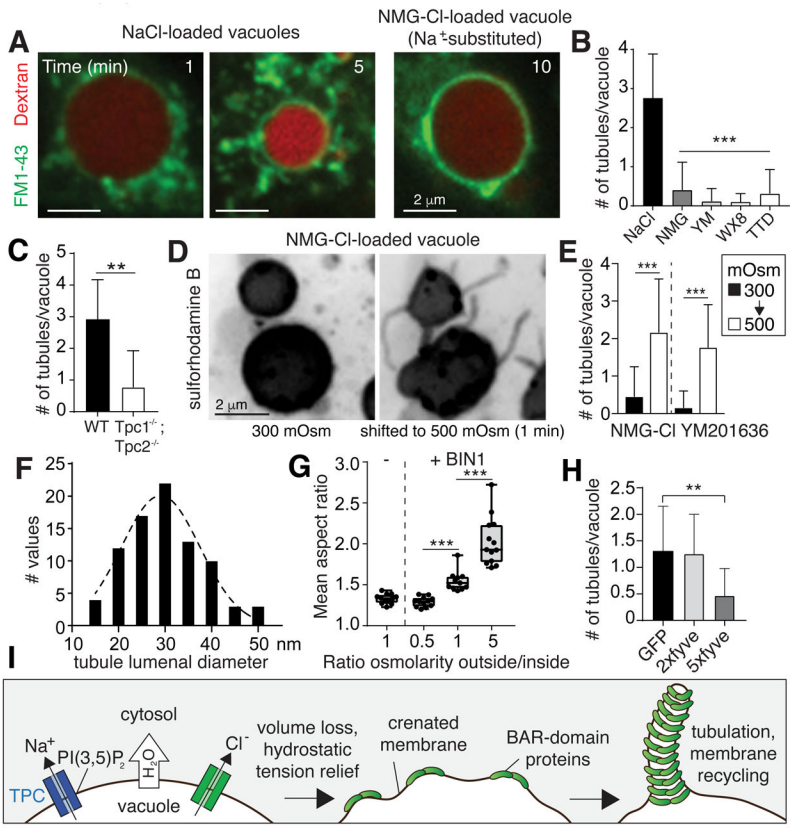


**Figure 3. Osmotically-driven shrinkage induces tubulation.**

**A**, BMDM were stimulated with M-CSF and the distribution of 70 kDa rhodamine-dextran and FM1-43 imaged at the indicated times after removal of the stimulus. **B-C**, Mean number of tubules (exceeding 1 μm in length) measured 5 min after stimulation with M-CSF; >100 macropinosomes (n=3) for each condition. **D-E**, Macropinosomes containing sulforhodamine B and N-methylglucamine chloride or formed in cells treated with YM201636 (500 nM) were recorded 10 min after formation, before and after being subjected to hypertonic solution. See also Video S5. >100 vacuoles, n=6. **F**, TEM was used to measure the diameter of tubules emerging from macropinosomes; 85 tubules quantified. **G**, Liposomes formed of whole brain lipid, rhodamine-labelled phosphatidylethanolamine, and PtdIns(4,5)$P_2$ in 20 mOsm solution. The mean aspect ratio for 3-5 fields of liposomes incubated with or without recombinant human BIN1 was quantified by imaging, n=3. **H**, HT1080 cells expressing GFP, 2xfyve-GFP, or 5xfyve-GFP were pulsed with SRB for 10 min. Mean number of tubules (exceeding 1 μm in length); >100 macropinosomes (n=3) for each condition. All *p* values determined by unpaired, two-sided t-tests. **I**, Model of mechanism proposed to underlie macropinosomal tubulation.

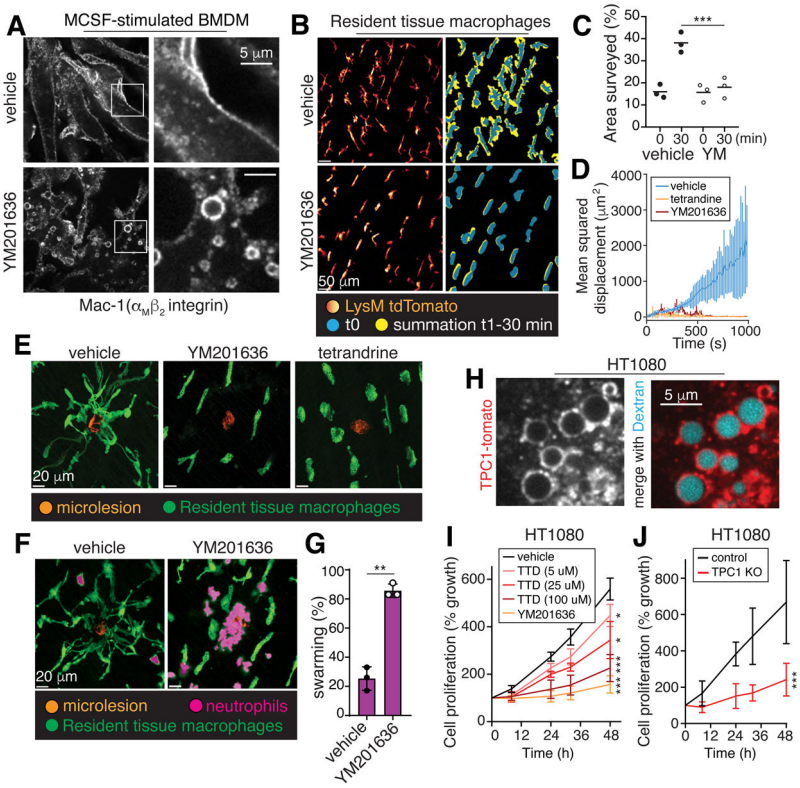


**Figure 4. Vacuolar resolution maintains cellular responsiveness and tissue surveillance.**

**A**, BMDM were stimulated for 30 min with M-CSF, with or without YM201636, fixed and immunostained for Mac-1. **B-E**, Resident tissue macrophages (LysM-tdTomato) with or without YM201636 or tetrandrine were stimulated with M-CSF for 10 min followed by removal of the stimulus for 30 min. Cells were then imaged for 30 min. **C**, surveillance area measured in the absence (left) or presence (right) of YM201636 (YM) over time, n=3. In **D-E**, 30 min after M-CSF removal, laser-induced microlesions were generated, marked by the resultant autofluorescence (orange in **E**). Mean squared displacement of the macrophages is graphed in **D**; means ± SD, n=3. Representative images in **E** taken at 15 min post-injury. **F-G**, Experiments performed as in **E**. Representative images denoting the presence of neutrophils are shown. In **G**, the % of lesions with neutrophil swarming was quantified for 6 microlesions per animal, n=3. **H**, HT1080 cells expressing TPC1-tomato were incubated with 70 kDa dextran for 10 min before imaging. **I-J**, wildtype and TPC1 KO HT1080 cell growth measured in the absence or presence of YM201636 or tetrandrine (TTD) by cell counting. Means ± SD, n=3. All *p* values determined by Mann-Whitney U tests.